Check for updates

Radio Science

RESEARCH ARTICLE
10.1029/2024RS008168

# Comparative Analysis of Performance for Optimization-Based Transionospheric SAR Autofocus

Mikhail Gilman[1] and Semyon Tsynkov[1]

[1]Department of Mathematics, North Carolina State University, Raleigh, NC, USA

**Key Points:**

- Optimization-based approach is applicable to the transionospheric synthetic aperture radar (SAR) autofocus; however, the minimization procedure is a hurdle
- Screen projection autofocus is an attractive alternative approach to transionospheric SAR autofocus that does not involve optimization
- The performance of the optimization-based SAR autofocus is found to be superior to the screen projection method

**Correspondence to:**
M. Gilman,
mgilman@ncsu.edu

**Citation:**
Gilman, M., & Tsynkov, S. (2025). Comparative analysis of performance for optimization-based transionospheric SAR autofocus. *Radio Science*, *60*, e2024RS008168. https://doi.org/10.1029/2024RS008168

Received 28 OCT 2024
Accepted 31 JAN 2025

**Abstract** For a spaceborne synthetic aperture radar (SAR) operating on low frequencies (such as P-band), turbulence in the Earth's ionosphere may cause significant phase perturbations of the interrogating signals. These perturbations depend on both the antenna and target coordinates and may lead to substantial image distortions. In our previous work, we proposed a variational approach to correcting the distortions that we called the transionospheric SAR autofocus. It required solving a complex optimization problem but performed well in numerical tests. As the optimization problem may be considered a hurdle, in the current work we compare the performance of the transionospheric SAR autofocus against that of a non-variational approach. The latter combines partial focusing with traditional autofocus where the phase perturbations are assumed to depend only on the antenna coordinates but not the target coordinates. In most cases, the optimization-based SAR autofocus produces images with better articulated peaks (i.e., peaks that are taller and narrower) as compared to those by the alternative approach.

## 1. Introduction

Synthetic aperture radar (SAR) imaging relies on accurate reconstruction of the phase history of radar signals reflected off the target. The phase history (or travel time history) is prone to perturbations of various origins. In particular, the ionospheric turbulence is a key source of phase perturbations for spaceborne SAR instruments (Garnier & Sølna, 2013; Gilman & Tsynkov, 2017; Gomba et al., 2015; Kim et al., 2015; Pi, 2015). If not compensated for, these phase perturbations may lead to significant distortions of the resulting SAR images. The mitigation of these distortions is known as SAR autofocus, the hardest part of which is estimation of the unknown perturbation function affecting the phases of the received radar signals.

Traditional autofocus for SAR corrects the phase perturbations due to disturbances of the antenna trajectory. A number of well-known methods, such as the map-drift and phase gradient autofocus (PGA), have been successfully used for decades. However, when phase perturbations are accumulated along the signal travel path, which is the case for transionospheric radar, these methods cannot be applied directly. The reason is that the phase correction generated by traditional autofocus (e.g., PGA) depends only on the antenna coordinate (slow time), whereas the signal path through the turbulent ionosphere (and hence, the accumulated phase perturbation) depends on both the antenna and target coordinates. As shown in Gilman and Tsynkov (2023b) and Kim et al. (2015), if the compensation of phase perturbations does not take into account their dependence on target coordinates, the residual distortions of images appear significant.

The interest to autofocus algorithms for transionospheric radars is motivated in part by the upcoming launch of the world's first satellite-based P-band SAR on the BIOMASS mission (Betancourt-Payan et al., 2022; Biomass ESA's forest mission, 2024; Heliere et al., 2014; Li et al., 2015), as well as the potential dual-use applications of low-frequency SAR. A recent review paper (Ji et al., 2024) emphasizes that the defocusing of SAR images due to the scintillation phase error (i.e., turbulent fluctuations of electron density in the ionosphere) "remains an intractable issue that has not been well mitigated by autofocus processing."

In our work (Gilman & Tsynkov, 2023b), we have developed a variational autofocus algorithm for transionospheric SAR imaging. It seeks to enhance the image sharpness by varying the parameters of the ionospheric phase correction built into the SAR signal processing procedure. Yet it is not equivalent to, say, the full waveform inversion where the image itself is obtained as a result of optimization. In Gilman and Tsynkov (2023b), the image is rather built using the conventional SAR reconstruction (matched filter and summation along the synthetic array) augmented with the correction of the unknown phase. The best focusing is then obtained by choosing the correction that would minimize a special sharpness-promoting cost function applied to the image.

© 2025. The Author(s).
This is an open access article under the terms of the Creative Commons Attribution-NonCommercial-NoDerivs License, which permits use and distribution in any medium, provided the original work is properly cited, the use is non-commercial and no modifications or adaptations are made.

19447799x, 2025, 2, Downloaded from https://agupubs.onlinelibrary.wiley.com/doi/10.1029/2024RS008168, Wiley Online Library on [22/02/2025]. See the Terms and Conditions (https://onlinelibrary.wiley.com/terms-and-conditions) on Wiley Online Library for rules of use; OA articles are governed by the applicable Creative Commons License

The phase correction for the methodology of Gilman and Tsynkov (2023b) is defined with the help of a phase screen. Phase screens are used routinely to model the effect of the ionosphere on the propagation of radar signals. A phase screen is a 2D surface (plane) positioned at a certain elevation above the Earth. A bivariate screen density function defined on the screen realizes the phase perturbations for the signals whose travel paths cross the screen. Thus, the screen allows for the dependence of perturbations on both the antenna and target coordinates. In work (Gilman & Tsynkov, 2023b), the screen density function represents the phase perturbations due to the ionospheric turbulence, and Fourier amplitudes of this function serve as control variables for optimization.

Of course, any phase screen is only an approximation aimed at simplifying the analysis. It replaces the graduate accumulation of phase perturbations along the signal travel path with a one-time jump at the intersection of the travel path with the screen. Therefore, the use of the phase screens for the analysis of specific ionospheric applications requires a justification. In Gilman and Tsynkov (2024), we provide a justification for employing the phase screens in the context of transionospheric autofocus. Also, the elevation of the screen is a key parameter of the formulation. It is often suggested that the screen be positioned in the region of the maximum electron concentration in the ionosphere. In Gilman and Tsynkov (2023a), we proposed a methodology (based on interferometric processing) for placing the screen where the ionosphere is most turbulent.

The transionospheric autofocus of Gilman and Tsynkov (2023b) has performed well in a variety of numerical tests. However, the optimization problem that needs to be solved in Gilman and Tsynkov (2023b) to enable good focusing is complex. It is non-convex (has multiple local minima), and computing the cost function could be numerically expensive. Therefore, one may be interested in looking for viable alternatives. It turns out though that unlike the plethora of well established traditional autofocus techniques aimed at correcting the SAR image distortions due to the antenna trajectory errors, very few methods have beed proposed in the literature specifically for correcting the distortions of spaceborne SAR images due to the ionospheric turbulence. The difficulty one needs to overcome is how to adequately take into account the dependence of phase perturbations not only on the antenna coordinates, but also the target coordinates.

A two-step focusing approach introduced in Ji et al. (2022) and Kim et al. (2015) aims at addressing this goal. The first step is transfer of the data to the phase screen level (this operation is also referred to as partial focusing). It is followed by the application of phase corrections to the transferred data by means of a conventional autofocus. The algorithm of Kim et al. (2015) uses the Faraday rotation angle to reconstruct the screen density and hence requires the polarimetric data. Work (Ji et al., 2022) adopts the traditional autofocus approach where the information from multiple range bins is combined in order to improve the performance in the presence of the clutter and noise. Neither of the two methods needs optimization, resulting in an easier numerical implementation. Yet no quantitative estimates of the corresponding focusing improvements were reported in either (Kim et al., 2015) or (Ji et al., 2022).

Thus, to compare the variational autofocus of Gilman and Tsynkov (2023b) against the two-step focusing of Ji et al. (2022), we need to conduct some additional analysis of the latter. We do this by considering the imaging operator of Ji et al. (2022). In particular, we find that in the absence of phase perturbations, the resolution of the system is the same as that for the standard SAR imaging. At the same time, when the phase perturbations are present, the two-step procedure cannot fully compensate for them and allows for residual distortions. We present an analytic estimate of those. Moreover, we perform a series of numerical simulations showing that the optimization-based method of Gilman and Tsynkov (2023b) yields better focused images than the two-step algorithm of Ji et al. (2022).

To guarantee that the comparison between the two methods is fair, we also need to make sure that both are applied to the same setting. For either (Gilman & Tsynkov, 2023b) or (Ji et al., 2022), we consider a closed-form autofocus problem, that is, assume that no external data about the phase screen are available. As far as the target, the two-step focusing method relies on using multiple range bins with exactly one dominant point scatterer in each. This is a typical requirement for the PGA [and, likewise, for its stripmap modification known as the phase curvature autofocus (PCA)], which is an essential part of the two-step method. In reality, however, this assumption does not hold, in particular, due to the clutter. The effect of the latter is suppressed by combining the phase information from multiple range bins (see (Jakowatz et al., 1996) for detail). Contrary to that, the optimization-based technique of Gilman and Tsynkov (2023b) does not require multiple bins and demonstrates good performance for a single bin with several scatterers in it. Yet one more difference between these two techniques is that they are formulated for different SAR imaging modes: stripmap versus spotlight for the

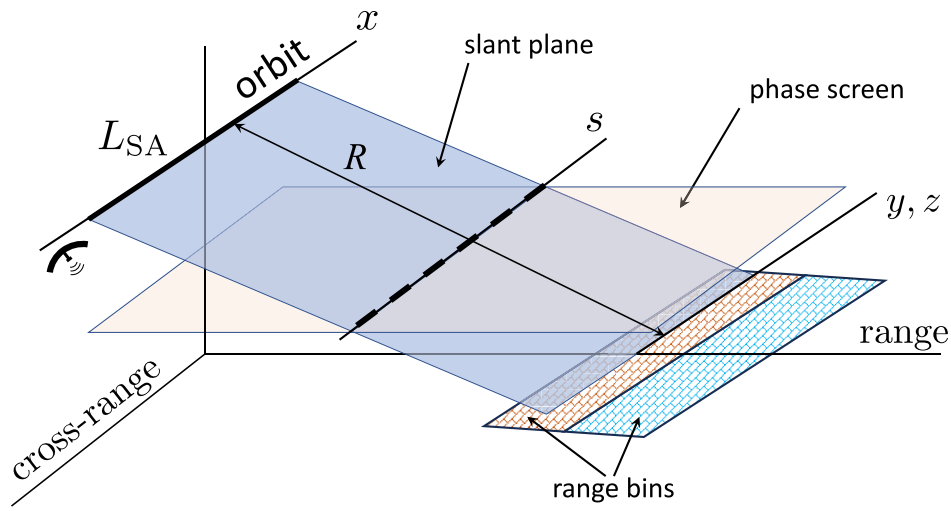


**Figure 1.** Three-dimensional geometry of transionospheric SAR imaging with a phase screen. Two adjacent range bins are shown. The azimuthal coordinates $y$, $z$, and $s$ are used as arguments of the image, scatterer reflectivity, and phase screen density function, respectively, whereas $x$ denotes the antenna position. Different range bins are distinguished by the index $k$, see Section 4; however, since the range coordinate is not essential in this work, there is no specific notation for it. The angles and distances are not to scale.

optimization based and two-step (also called screen projection) methods, respectively. Thus, to put both methods on the same footing, we extend the optimization-based approach of Gilman and Tsynkov (2023b) to work with multiple range bins and replace PGA with PCA for the screen projection method to work with the stripmap data. Then, the performance of each autofocus methodology is evaluated and compared to one another using the statistics of the relevant image sharpness metrics, such as the integrated sidelobe ratio (ISLR) and height of the peak due to a point scatterer.

The analysis in this paper is performed for the range-compressed setting and stripmap imaging mode as described in Gilman and Tsynkov (2023a, 2023b), see also Figure 1. Unlike in Ji et al. (2022) and Kim et al. (2015), we use the time domain in the azimuthal direction; this makes it easier to analyze the geometry of rays in a slant plane. The details of the problem setup are given in Section 2. Section 3 discusses the properties of the SAR imaging operator in the presence of phase perturbations realized by means of a phase screen. We formulate the autofocus problem with multiple range bins in Section 4. The optimization-based approach is described in Section 5, while the two-step algorithm is outlined in Section 6. In Section 7, we run a series of numerical experiments to compare the performance of the two methods. Section 8 summarizes the results of the study.

## 2. Governing Equations

In this section, we consider a range compressed domain associated with a single range bin. We also introduce the corresponding slant plane, see Figure 1. The reflectivity, SAR image, and phase screen density are represented by univariate functions (see (Gilman & Tsynkov, 2023a; Gilman & Tsynkov, 2023b) for more detail). For the stripmap SAR imaging subject to phase distortions, the range-compressed antenna signal $u(x)$ is expressed via the reflectivity in the range bin $\mu(z)$ as follows:

$$u(x) = \int_{x-F/2}^{x+F/2} \exp\left(\mathrm{i}\pi(x-z)^2/F\right) \cdot \exp\left[-\mathrm{i}\Psi(s(x,z))\right] w_u(x-z)\mu(z)\,\mathrm{d}z, \tag{1}$$

while the regular SAR image $\mathcal{I}_1(y)$ is obtained from $u(x)$ by one-step reconstruction using a matched filter:

$$\mathcal{I}_1(y) = \frac{1}{F}\int_{y-F/2}^{y+F/2} \exp\left(-\mathrm{i}\pi(x-y)^2/F\right) \cdot \exp\left[\mathrm{i}\Psi^{\mathrm{rec}}(s(x,y))\right] w_{\mathcal{I}}(x-y)u(x)\,\mathrm{d}x. \tag{2}$$



1944799x, 2025, 2, Downloaded from https://agupubs.onlinelibrary.wiley.com/doi/10.1029/2024RS008168, Wiley Online Library on [22/02/2025]. See the Terms and Conditions (https://onlinelibrary.wiley.com/terms-and-conditions) on Wiley Online Library for rules of use; OA articles are governed by the applicable Creative Commons License

1944799x, 2025, 2, Downloaded from https://agupubs.onlinelibrary.wiley.com/doi/10.1029/2024RS008168, Wiley Online Library on [22/02/2025]. See the Terms and Conditions (https://onlinelibrary.wiley.com/terms-and-conditions) on Wiley Online Library for rules of use; OA articles are governed by the applicable Creative Commons License

The complete derivation of Equations 1 and 2 can be found in Gilman and Tsynkov (2023a), Appendix A. In particular, the dimensionless azimuthal coordinates $x$, $y$, $z$, and $s$ are normalized by the resolution size $\Delta_{\mathrm{A}}$ given by

$$\Delta_{\mathrm{A}} = \pi Rc/(\omega_0 L_{\mathrm{SA}}). \tag{3}$$

The quantity $F = L_{\mathrm{SA}}/\Delta_{\mathrm{A}} \gg 1$ is the dimensionless length of the synthetic aperture. Further, $R$ is the distance between the antenna track and the target (also called distance of closest approach), $c$ is the speed of light, and $\omega_0 = 2\pi f_0$ is the radar carrier frequency. The unknown phase screen density $\Psi(s)$, as well as the reconstruction phase $\Psi^{\mathrm{rec}}(s)$, are functions of the screen coordinate $s$, which, in turn, is a function of the orbit and ground coordinates:

$$s(x,z) = \xi x + (1-\xi)z, \tag{4}$$

where $\xi$ is the ratio of the screen and orbit altitudes such that $0 \le \xi \le 1$. Hereafter, $\xi$ is assumed known (see, for example, (Gilman & Tsynkov, 2023a)). Finally, $w_u(\cdot)$ and $w_I(\cdot)$ are the window functions that will be taken the same:

$$w_u \equiv w_I \equiv w.$$

In this work, we consider either rectangular or parabolic windows:

$$w(x) \equiv w^{\mathrm{rect}}(x) = \begin{cases} 1, & \text{if} \quad |x| \le F/2, \\ 0, & \text{otherwise}, \end{cases} \tag{5a}$$

$$w(x) \equiv w^{\mathrm{parab}}(x) = w^{\mathrm{rect}}(x)\left(1 - 4\frac{x^2}{F^2}\right). \tag{5b}$$

The phase perturbation $\Psi(s)$ in Equation 1 is represented by means of a finite Fourier series:

$$\Psi(s) = \mathrm{Re}\sum_{n=1}^{N} a_n \exp\left(\mathrm{i}k_n s + \mathrm{i}\varphi_n\right) = \sum_{n=1}^{N}\left(p_n \cos(k_n s) + q_n \sin(k_n s)\right), \tag{6}$$

where $a_n > 0$, $k_n > 0$, $\varphi_n$, $p_n$, and $q_n$ are real.

The $L_2$ norm of $\Psi$, referred to as magnitude of perturbations, is an important parameter that determines the level of image distortions:

$$a_s = \left(\sum_{n=1}^{N} a_n^2\right)^{1/2}. \tag{7}$$

It depends on the ionospheric conditions, as well as the radar carrier frequency $\omega_0$. For a P-band radar, the values of $a_s \gtrsim \pi$ correspond to a high level of image distortions (Gilman & Tsynkov, 2023b; Gilman et al., 2017). Note that in the context of transionospheric SAR imaging, the level of ionospheric distortions is often characterized by the quantity known as $\mathrm{C_kL}$, whereas in this work, the level of distortions is given by the magnitude of the perturbation phase given by Equation 7. To obtain a relation between these two descriptions, in our earlier work (Gilman & Tsynkov, 2023b, Appendix A) we used the Rino scintillation model, see (Rino, 1979, Formula 19), and certain realistic values of the ionospheric parameters (Meyer et al., 2016), in particular, $\nu = 3$ and $r_0 = 5$ km for the spectral index and outer scale of the ionospheric turbulence, respectively. For $a_s = 2\pi$ typical to both (Gilman & Tsynkov, 2023b) and this publication, we found the corresponding $\mathrm{C_kL}$ to be about $10^{32}$. This value is relatively high, see, for example, (Secan & Bussey, 1994), but even higher values of $\mathrm{C_kL}$ have also been reported in the literature and used in the context of transionospheric SAR imaging, see (Carrano et al., 2012; Ji et al., 2022; Meyer et al., 2016; Reeves et al., 2019).

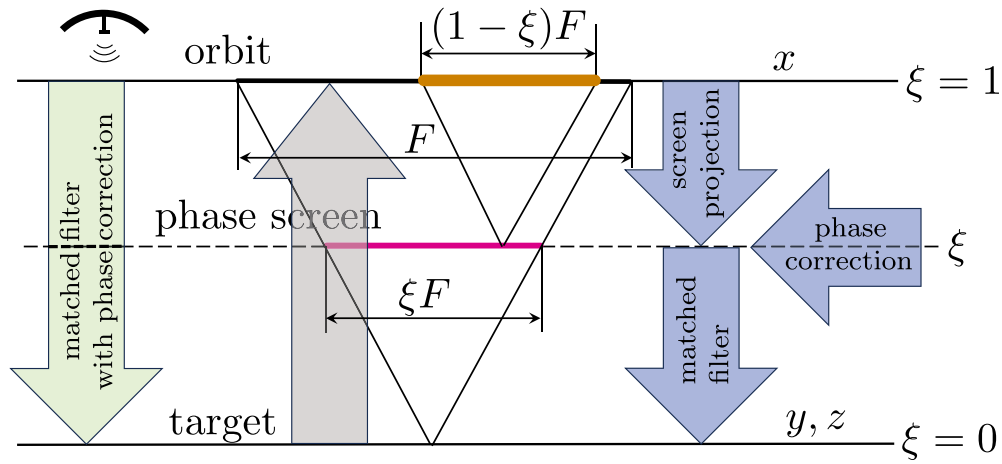


**Figure 2.** Data flow for the traditional one-step SAR imaging (green block arrow, see Equation 2) and two-step imaging that involves screen projection (blue block arrows, see Equations 8 and 9), with the apertures for the first and second steps highlighted. The gray upward-pointing block arrow is common for both scenarios and corresponds to Equation 1.

In the two-step approach of Ji et al. (2022) and Kim et al. (2015), also called screen projection method, the reconstruction Equation 2 is replaced with the following two:

$$p(s) = \frac{1}{\eta F}\int_{s-\eta F/2}^{s+\eta F/2} \exp\left(-\mathrm{i}\pi(x-s)^2/(\eta F)\right) w(x-s)u(x)\,\mathrm{d}x, \tag{8}$$

$$\mathcal{I}_2(y) = \frac{1}{\xi F}K_2\int_{y-\xi F/2}^{y+\xi F/2} \exp\left(-\mathrm{i}\pi(y-s)^2/(\xi F)\right) \exp\left(\mathrm{i}\Psi^{\mathrm{rec}}(s)\right) w(y-s)p(s)\,\mathrm{d}s, \tag{9}$$

where $\eta = 1 - \xi$, and $K_2$ is a normalization constant defined later in Equation 19. Each of the two steps given by Equations 8 and 9 is similar to the full reconstruction given by Equation 2, but with the following modifications. At the first step (8), also called the screen projection, the reconstruction phase $\Psi^{\mathrm{rec}}$ is not present and the distances are scaled as $(R, L_{\mathrm{SA}}) \to (\eta R, \eta L_{\mathrm{SA}})$, see Figure 2. It is this similarity that allows one to interpret the new function $p(s)$ defined by Equation 8 as "data transferred to the screen elevation" or "partially focused image," see (Ji et al., 2022; Kim et al., 2015). At the second step (9), the scaling of the distances is $(R, L_{\mathrm{SA}}) \to (\xi R, \xi L_{\mathrm{SA}})$ and the reconstruction phase $\Psi^{\mathrm{rec}}(s)$ is merged with $p(s)$ into the "corrected signal," $\exp\left(\mathrm{i}\Psi^{\mathrm{rec}}(s)\right) p(s)$. The data flow schematic for the one-step and two-step imaging techniques is shown in Figure 2. Further justification for using the transforms (8) and (9) instead of the standard matched filter (2) is provided in Section 3, see Equations 17–19 and the discussion around them.

The advantage of the two-step formulation (8)–(9) is that unlike in (2), the perturbation term in (9) is similar to that due to the antenna trajectory errors. Hence, traditional SAR autofocus algorithms that do not require optimization (such as PGA or PCA, see (Jakowatz et al., 1996; Wahl et al., 1994)) can be applied to derive $\Psi^{\mathrm{rec}}$.

## 3. SAR Imaging Operator in the Presence of Phase Perturbations

The relation between the image $\mathcal{I}_1$ and reflectivity $\mu$ given by Equations 1 and 2, as well as the relation between $\mathcal{I}_2$ and $\mu$ expressed by Equations 1, 8, and 9, can be represented as integral operators:

$$\mathcal{I}_\alpha(y) = \int_{-\infty}^{\infty} W_\alpha(y, z)\mu(z)\,\mathrm{d}z, \quad \alpha \in \{1, 2\}, \tag{10}$$

also called the imaging operators. For the simplest case of rectangular windows, see Equation 5a, the imaging kernels $W_\alpha$ can be expressed as follows:



1944799x, 2025, 2, Downloaded from https://agupubs.onlinelibrary.wiley.com/doi/10.1029/2024RS008168, Wiley Online Library on [22/02/2025]. See the Terms and Conditions (https://onlinelibrary.wiley.com/terms-and-conditions) on Wiley Online Library for rules of use; OA articles are governed by the applicable Creative Commons License

$$W_1 = \frac{1}{F}\int_{\mathcal{D}_1} \exp\left(\mathrm{i}\phi_1 + \mathrm{i}\phi_{1,\Psi}\right) \mathrm{d}x, \tag{11a}$$

$$W_2 = \frac{1}{\xi\eta F^2} K_2 \iint_{\mathcal{D}_2} \exp\left(\mathrm{i}\phi_2 + \mathrm{i}\phi_{2,\Psi}\right) \mathrm{d}x\, \mathrm{d}s_\mathrm{d}, \tag{11b}$$

where

$$\mathcal{D}_1 = \{x \mid (|x - z| \le F/2) \cap (|x - y| \le F/2)\}, \tag{12a}$$

$$\mathcal{D}_2 = \{(x, s_\mathrm{d}) \mid (|x - z| \le F/2) \cap (|x - s_\mathrm{d}| \le \eta F/2) \cap (|s_\mathrm{d} - y| \le \xi F/2)\}. \tag{12b}$$

In Equations 11b and 12b, we used $s_\mathrm{d}$ instead of $s$ to avoid confusion with $s(x, z)$ in Equation 1.

In Equation 11, the phases $\phi_1$ and $\phi_2$ are due to the propagation terms and matched filters in Equations 1, 2, 8, and 9 and hence do not contain $\Psi$ or $\Psi^\mathrm{rec}$. The phase $\phi_1$ is represented as

$$\phi_1 = \frac{2\pi}{F}(y - z)\left(x - \frac{y + z}{2}\right). \tag{13}$$

For $|y - z| \lesssim 1$, the length of the interval $\mathcal{D}_1$ defined in Equation 12a is close to $F$, and the integration in Equation 11a when $\phi_{1,\Psi} = 0$ (i.e., in the absence of perturbations) yields the familiar sinc expression for the imaging kernel:

$$W_1(y, z)|_{\Psi = \Psi^\mathrm{rec} = 0} \approx \mathrm{sinc}(\pi(y - z)), \quad \text{where} \quad \mathrm{sinc}\,\zeta \overset{\mathrm{def}}{=} \frac{\sin\zeta}{\zeta}. \tag{14}$$

For $|y - z| \gg 1$, the phase $\phi_1$ given by Equation 13 leads to fast oscillations under the integral in Equation 11a. Therefore, we will have $|I_1| \ll 1$ far away from strong scatterers.

The second term under the exponential on the right-hand side of Equation 11a, $\phi_{1,\Psi}$, accounts for phase distortions. To estimate the residual phase distortions in the case of an ideal reconstruction, that is, when $\Psi^\mathrm{rec} = \Psi$ in Equation 2, we introduce a dimensionless spatial scale $L_\Psi$ of turbulence-induced phase perturbations and assume that $1 \ll L_\Psi \ll F$. Then, we can approximate $\phi_{1,\Psi}$ by Taylor's formula for $|y - z| \lesssim 1$:

$$\begin{aligned} \phi_{1,\Psi} &= \Psi^\mathrm{rec}(s(x, y)) - \Psi(s(x, z)) = \Psi(s(x, y)) - \Psi(s(x, z)) \\ &\approx \Psi'(s(x, z)) \cdot (s(x, y) - s(x, z)) \approx \eta\Psi'(s(x, z)) \cdot (y - z). \end{aligned} \tag{15}$$

Consequently, for the average absolute value of $\phi_{1,\Psi}$ we can write:

$$\overline{|\phi_{1,\Psi}|} \sim \eta\frac{a_s}{L_\Psi}. \tag{16}$$

Carrying out an analysis similar to Equations 13–16 for $W_2$ given by Equation 11b would be more difficult because of a complicated geometry of $\mathcal{D}_2$ in Equation 12b. We thus simplify the scenario: take $\Psi(s) = \Psi^\mathrm{rec}(s) = 0$, $\mu(z) = \mu_0\delta(z - z_0)$, and substitute Equation 1 into Equation 8. This yields:

$$\begin{aligned} p_\mathrm{clean}(s_\mathrm{d}) &\approx \mu_0 \exp\left(i\pi q^2/F\right) \int_{-1/2}^{1/2} \exp\left(2\mathrm{i}\pi\eta q\check{x} - \mathrm{i}\pi\eta\xi F\check{x}^2\right) \mathrm{d}\check{x} \\ &\approx \frac{\mu_0}{\sqrt{\xi\eta F}} \exp\left(\frac{\mathrm{i}\pi q^2}{\xi F} - \frac{\mathrm{i}\pi}{4}\right), \end{aligned} \tag{17}$$

where $\check{x} = (x - s_\mathrm{d})/(\eta F)$ and $q = s_\mathrm{d} - z_0$, $|q| \le \xi F/2$. The last approximation in Equation 17 is obtained using the method of stationary phase under the assumptions $F \gg |q|$ and $\eta F \gg 1$. Up to a constant factor of



1944799x, 2025, 2, Downloaded from https://agupubs.onlinelibrary.wiley.com/doi/10.1029/2024RS008168, Wiley Online Library on [22/02/2025]. See the Terms and Conditions (https://onlinelibrary.wiley.com/terms-and-conditions) on Wiley Online Library for rules of use; OA articles are governed by the applicable Creative Commons License

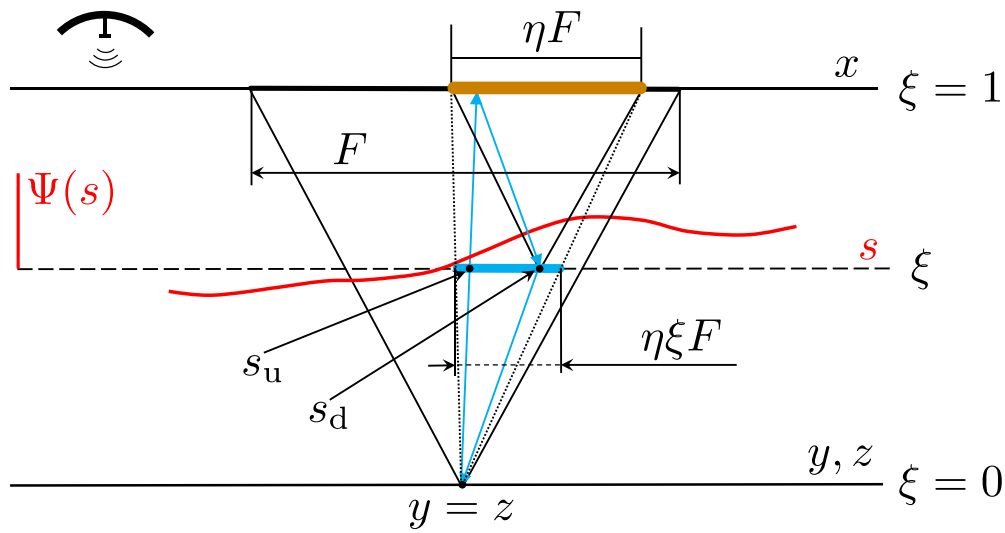


**Figure 3.** The geometry of rays for the two-step reconstruction. The red curve illustrates the screen density function $\Psi(s)$. The blue arrows illustrate the rays involved in the transforms Equations 1, 8, and 9 for the case of $y = z$. The domain of all relevant values of $s_u$ for a given $s_d$ is shown by a thick horizontal blue line. The angles and distances are not to scale.

$(\xi\eta F)^{-1/2} \exp(-i\pi/4)$, the expression on the right-hand side of Equation 17 coincides with an unperturbed signal due to the point scatterer $\mu(z) = \mu_0\delta(z - z_0)$ in the case of antenna at screen elevation. This signal can be obtained by setting $\Psi = 0$ in Equation 1, replacing $F$ with $\xi F$ and trajectory variable $x$ with screen variable $s$, using the rectangular window given by Equation 5a, and substituting $\mu(z) = \mu_0\delta(z - z_0)$:

$$u_\xi(s) = \int_{s-\xi F/2}^{s+\xi F/2} \exp\left(i\pi(s-z)^2/\xi F\right)\mu_0\delta(z-z_0)\,dz = \mu_0 \exp\left(\frac{i\pi(s-z_0)^2}{\xi F}\right). \tag{18}$$

Equation 18 holds for $|s - z_0| \le \xi F/2$. We also see that the right-hand side of Equation 17 is an azimuthal chirp with the rate $\pi(\xi F)^{-1}$. Hence, the first exponential term in the integrand of Equation 9 is a correct matched filter formulation for the "signal" $p_{\text{clean}}(s_d)$ given by Equation 17, and by choosing the normalization factor in Equation 11b as

$$K_2 = \sqrt{\xi\eta F}\exp(i\pi/4), \tag{19}$$

we arrive at

$$W_2(y,z)|_{\Psi=\Psi^{\text{rec}}=0} \approx W_1(y,z)|_{\Psi=\Psi^{\text{rec}}=0} \approx \text{sinc}(\pi(y-z)),$$

see Equation 14. This means, in particular, that in the absence of phase perturbations, the resolution of the two-step method, as formulated in Equations 8 and 9, is the same as that of the conventional reconstruction using Equation 2.

To estimate $\phi_{2,\Psi}$ in Equation 11b, we consider the case of $y = z$ and introduce $s_u = s(x,z)$, see Equation 4 and Figure 3. Then, the phase $\phi_{2,\Psi}$ can be expressed as

$$\phi_{2,\Psi} = \Psi^{\text{rec}}(s_d) - \Psi(s_u),$$

where $\Psi^{\text{rec}}(s_d)$ and $\Psi(s_u)$ come from Equations 1 and 9, respectively. Accordingly, the factor $(s(x,y) - s(x,z))$ in Equation 15 is replaced with $s_d - s_u$. The typical values of $|s_d - s_u|$ are of the order of $\xi\eta F$, which is the size of the domain of all $s_u$ for a fixed $s_d$ (in Figure 3, this domain is shown by a thick horizontal blue line). Specifically, the value of $|s_d - s_u|$ averaged over all $(s_d, s_u)$ is given by



1944799x, 2025, 2, Downloaded from https://agupubs.onlinelibrary.wiley.com/doi/10.1029/2024RS008168, Wiley Online Library on [22/02/2025]. See the Terms and Conditions (https://onlinelibrary.wiley.com/terms-and-conditions) on Wiley Online Library for rules of use; OA articles are governed by the applicable Creative Commons License

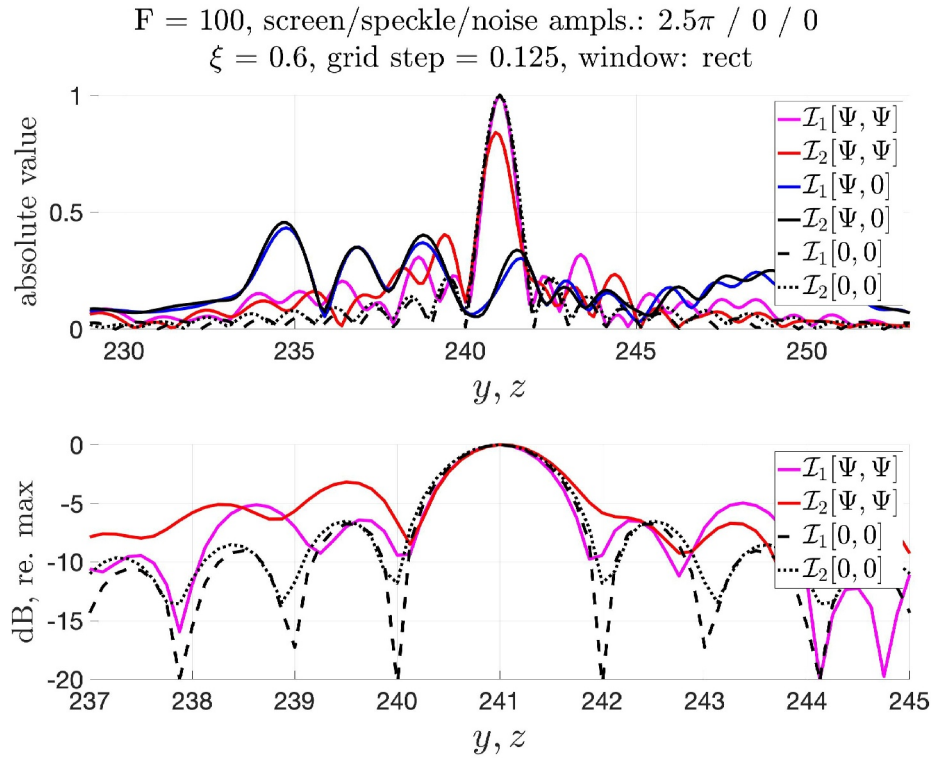


**Figure 4.** SAR images due to a point scatterer $\mu(z) = \delta(z - z_0)$. The notations $\mathcal{I}_\alpha[\Psi, \Psi]$ and $\mathcal{I}_\alpha[\Psi,0]$, $\alpha \in \{1,2\}$, see Equation 10, correspond to $\Psi^{\text{rec}} = \Psi$ and $\Psi^{\text{rec}} = 0$, respectively, whereas $\mathcal{I}_\alpha[0,0] \approx \text{sinc}(y - 241)$ is the unperturbed case: $\Psi^{\text{rec}} = \Psi = 0$, see Equation 14. The perturbation level is high: $a_s = 2.5\pi$. On the decibel (i.e., lower) panel, the plot for $\mathcal{I}_2[\Psi, \Psi]$ is shifted horizontally to make its maximum position coincide with that of $\mathcal{I}_1[\Psi, \Psi]$. The unit along the horizontal axis is the resolution size $\Delta_{\text{A}}$, see Equation 3.

$$\overline{|s_{\text{d}} - s_{\text{u}}|} = K_s \cdot \xi\eta F, \tag{20}$$

where $K_s$ is a factor of order one that may also depend on $\xi$. For $\xi = \eta = 0.5$, it is easy to show that $K_s = 1/3$, and we assume that for other realistic values of $\xi$ this factor does not change significantly. Taking into account that the right-hand side of Equation 20 may exceed the valid range of arguments for the Taylor's formula used in Equation 15, we can write:

$$\overline{|\phi_{2,\Psi}|} \sim \min\left(\frac{a_s}{L_\Psi} K_s \xi\eta F,\ a_s,\ 2\pi\right). \tag{21}$$

For realistic magnitudes $a_s$, Equation 21 yields a significantly larger estimate of the residual phase distortions as compared to Equation 16. In other words, even for a perfect reconstruction of the screen density, that is, for $\Psi^{\text{rec}} = \Psi$, the compensation of phase perturbations in the two-step reconstruction procedure Equations 8 and 9 appears much less accurate than that in the one-step procedure of Equation 2. We will refer to this effect as corruption of the screen projected data. It takes place when the signal $u(x)$ is transferred to the screen level by means of Equation 8, see Appendix A.

The plots in Figure 4 show several examples of SAR images $\mathcal{I}_1$ and $\mathcal{I}_2$ for various scenarios. In the case of a perfect reconstruction, $\Psi^{\text{rec}} \equiv \Psi$, the peak due to a point scatterer in $\mathcal{I}_1$ appears sharper than that in $\mathcal{I}_2$ in terms of both its width and level of sidelobes. This corroborates numerically the foregoing analysis of the residual phase distortions. Moreover, it is well known that an uncompensated phase perturbation linear in azimuth (also called trend or phase ramp) results in a shift of the image as a whole, see, for example, (Gilman & Tsynkov, 2017; Jakowatz et al., 1996). Hence, the shift of the peak of $\mathcal{I}_2[\Psi, \Psi]$ observed in the top panel of Figure 4 can be seen as



1944799x, 2025, 2, Downloaded from https://agupubs.onlinelibrary.wiley.com/doi/10.1029/2024RS008168, Wiley Online Library on [23/02/2025]. See the Terms and Conditions (https://onlinelibrary.wiley.com/terms-and-conditions) on Wiley Online Library for rules of use; OA articles are governed by the applicable Creative Commons License

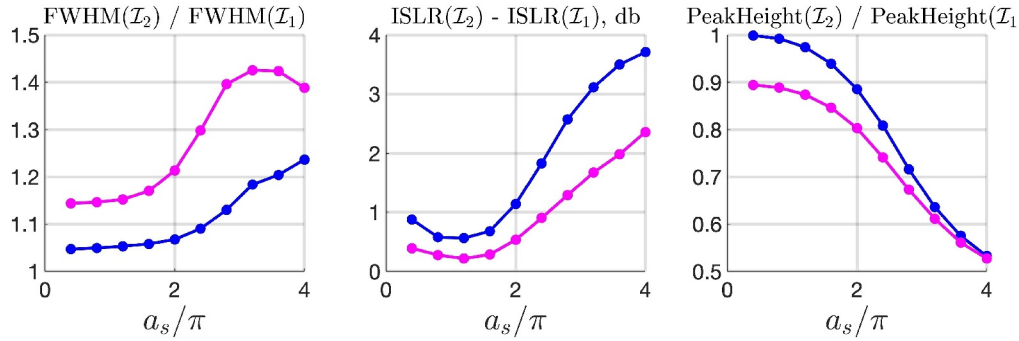


**Figure 5.** Comparison of average peak sharpness metrics for $\mathcal{I}_1$ and $\mathcal{I}_2$ for various perturbation magnitudes. The blue and purple curves correspond to the rectangular and parabolic windows, respectively, see Equation 2.

evidence of inaccurate reconstruction of the large-scale part of $\Psi^{\text{rec}}$ in the two-step alogirithm, resulting in a non-zero average of $[\Psi(s) - \Psi^{\text{rec}}(s)]'$ over the interval of $s$ around $s = 241$.

To quantify the (detrimental) effect of signal corruption on the screen projection approach, we perform a simulation where we vary the magnitude of phase perturbations by taking several different values of $a_s$ in Equation 7. For each specific $a_s$, we generate 10 realizations of the screen density function $\Psi(s)$ by choosing a random set of i.i.d. phases $\varphi_n$ in Equation 6, all uniformly distributed on $[0, 2\pi)$. For each $\Psi(s)$, we create 30 targets $\mu(z)$ with a randomly located point scatterer, and then build the images $\mathcal{I}_1$ and $\mathcal{I}_2$ using the ideal reconstruction, that is, $\Psi^{\text{rec}} = \Psi$. We calculate the following three common peak metrics for the resulting images: full width at half magnitude (FWHM), integrated sidelobe ratio (ISLR), and peak height. The plots of these metrics averaged over all screen realizations and point scatterer locations are presented in Figure 5. We see that as the magnitude $a_s$ increases, the sharpness metrics of the peaks in $\mathcal{I}_2$ deteriorate more rapidly as compared to those of $\mathcal{I}_1$, especially in terms of ISLR. Note that in the framework of our mathematical model, the ideal reconstruction $\Psi^{\text{rec}} = \Psi$ requires no autofocus as we merely set the reconstruction phase $\Psi^{\text{rec}}$ equal to the original phase perturbation $\Psi$ (that cannot be assumed known in a real-life setting). Yet the ideal reconstruction $\Psi^{\text{rec}} = \Psi$ can be thought of as the best possible outcome of any autofocus algorithm. Hence, we conclude that even in the best case scenario, the image quality of $\mathcal{I}_2$ shall be expected to be inferior to that of $\mathcal{I}_1$.

## 4. Autofocus With Multiple Range Bins

As in practice the phase perturbation $\Psi$ is not known, an autofocus algorithm shall be developed and implemented that would generate a reconstruction phase $\Psi^{\text{rec}}(s) \approx \Psi(s)$ and thus yield a well-focused image $\mathcal{I}_1(y)$ or $\mathcal{I}_2(y)$. Different autofocus methodologies require different amounts of data. Traditional methods such as PGA and PCA (the latter is used at the second step of the two-step approach, see Equation 9) need multiple range bins to enable iterative refinement and average out the effects of clutter and noise (Section 6). These methods work well when each range bin contains a single strong point scatterer. In contrast, the optimization-based autofocus of Gilman & Tsynkov (2023b) works with a single range bin and arbitrary number of scatterers. To make a fair comparison between the two methods, we have extended the optimization-based approach to the case of multiple range bins (see Section 5), where the reflectivity function in each bin contains exactly one strong point scatterer plus clutter. This is a preferred scenario for the two-step method because its second step relies on PCA.

Let the range bins be indexed by $k$, $1 \le k \le K$. We generate a set of reflectivity functions $\{\mu^{(k)}(z)\}$ that give rise to the antenna signals $\{u^{(k)}(x)\}$. The realizations of $\{\mu^{(k)}(z)\}$ and $\{u^{(k)}(x)\}$ for different values of $k$ represent different range bins of a SAR image, similarly to the traditional PGA (Jakowatz et al., 1996, Section 4.5). Note that in the actual 3D geometry with a phase screen, the interrogating and reflected signals for different range bins cross the screen at different locations, see Figure 1. However, the minimal spacing between the reference range coordinates of those bins is of the order of the range resolution, which is much shorter than the typical spatial scale of ionospheric turbulence. This allows us to assume one and the same $\Psi(s)$ in the signal model (1) and, similarly, use a single $\Psi^{\text{rec}}(s)$ in the reconstruction algorithm (2),(4) or (8),(9) for the entire set $\{u^{(k)}\}$. This setup is an extension of the one in Gilman and Tsynkov (2023b) where a single range bin was considered.



1944799x, 2025, 2, Downloaded from https://agupubs.onlinelibrary.wiley.com/doi/10.1029/2024RS008168, Wiley Online Library on [22/02/2025]. See the Terms and Conditions (https://onlinelibrary.wiley.com/terms-and-conditions) on Wiley Online Library for rules of use; OA articles are governed by the applicable Creative Commons License

To define the speckle and noise in $\{\mu^{(k)}(z)\}$ and $\{u^{(k)}(x)\}$, we first introduce $n^C$ as a complex-valued random vector with dimension equal to that of the discretization of quadratures in Equations 1 and 2. The real and imaginary parts of $n^C$ are arrays of independent standard Gaussian variables, and two different realizations of $n^C$, called $n^C_{\text{clutter}}$ and $n^C_{\text{noise}}$, will be used to define the speckle and noise in each bin. We will denote the intensity of the clutter and noise by $a_{\text{clutter}} \geq 0$ and $a_{\text{noise}} \geq 0$, respectively. The reflectivity in each bin is defined by

$$\mu^{(k)}_{\text{clutter}}(z) = a_{\text{clutter}} \cdot \left(\frac{d}{2}\right)^{1/2} \cdot n^C_{\text{clutter}}, \tag{22}$$

$$\mu^{(k)}(z) = m^{(k)}\delta\left(z - z^{(k)}\right) + \mu^{(k)}_{\text{clutter}}(z). \tag{23}$$

In Equation 22, $d$ is the discretization grid size, whereas $z^{(k)}$ and $m^{(k)}$ in Equation 23 are the coordinate and (complex) amplitude of the point scatterer in the $k$-th range bin. This normalization aims at equalizing the magnitudes of the antenna signals $u(x)$ due to the clutter and due to a point scatterer is the case where the intensities are equal: $a_{\text{clutter}} = |m^{(k)}|$. Altogether, the forward model for multiple bins is as follows:

$$\begin{aligned} u^{(k)}_{\text{signal}}(x) &= \int_{x-F/2}^{x+F/2} \exp\left(\mathrm{i}\pi(x-z)^2/F\right) \cdot \exp\left[-\mathrm{i}\Psi(s(x,z))\right]\mu^{(k)}(z)\,\mathrm{d}z, \\ u^{(k)}_{\text{noise}}(x) &= a_{\text{noise}} \cdot \left(\frac{1}{2}\right)^{1/2} \cdot \max\left(\left|u^{(k)}_{\text{signal}}(x)\right|\right) \cdot n^C_{\text{noise}}, \\ u^{(k)}(x) &= u^{(k)}_{\text{signal}}(x) + u^{(k)}_{\text{noise}}(x). \end{aligned} \tag{24}$$

The images $\mathcal{I}^{(k)}_1(y)$ for each bin are obtained by applying Equation 2 to $u^{(k)}$ of Equation 24, whereas to obtain $\mathcal{I}^{(k)}_2(y)$, Equations 8 and 9 are applied to Equation 24 instead. Both methods require the reconstruction phase $\Psi^{\text{rec}}(s)$ that will be derived using one of the two autofocus approaches presented in Sections 5 and 6.

## 5. Optimization-Based Autofocus

In Gilman and Tsynkov (2023b), we have developed and tested a variational autofocus methodology where the reconstruction phase $\Psi^{\text{rec}}(s)$ was represented as a finite Fourier sum, similar to $\Psi(s)$ of Equation 6:

$$\Psi^{\text{rec}}(s) = \sum_{n=1}^{N^{\text{rec}}} \left(p^{\text{rec}}_n \cos\left(k^{\text{rec}}_n s\right) + q^{\text{rec}}_n \sin\left(k^{\text{rec}}_n s\right)\right). \tag{25}$$

The original perturbation spectrum in Equation 6 and reconstruction spectrum in Equation 25 can be the same or they can be different, and we have shown in Gilman and Tsynkov (2023b) that the optimization-based autofocus works well in either case. In this work, for simplicity, we use the same wavenumber spectra for the perturbation and reconstruction phase: $N^{\text{rec}} = N$ and $k^{\text{rec}}_n = k_n$ for all $n$. The output of the autofocus procedure is a set of the Fourier amplitudes: $\left\{\left(p^{\text{rec}}_n, q^{\text{rec}}_n\right),\ n = 1, \ldots, N^{\text{rec}}\right\}$; using these values in Equation 25, we can calculate $\Psi^{\text{rec}}(s)$ for any value of $s$. Examples of such reconstruction will be presented in Figures 8 and 9.

In the variational approach of Gilman and Tsynkov (2023b), we considered a single range bin, that is, $K = 1$, and employed a sharpness-enhancing cost function $\text{Cost}_{\mathcal{I}}[\mathcal{I}_1] = -\|\mathcal{I}_1\|^4_4$ that has appeared previously in Fienup and Miller (2003), Morrison et al. (2007), Muller and Buffington (1974), and Tippie and Fienup (2009). The control variables for optimization were $p^{\text{rec}}_n$ and $q^{\text{rec}}_n$. A regularization term $\text{Cost}_\Psi[\Psi^{\text{rec}}] = \zeta\|(\Psi^{\text{rec}})'\|^2_2$ was added to the cost function, where the value of the weight $\zeta = 0.7$ was chosen experimentally. For the purpose of implementation, the overall cost function $\text{Cost}[\mathcal{I}_1, \Psi^{\text{rec}}] = \text{Cost}_{\mathcal{I}}[\mathcal{I}_1] + \text{Cost}_\Psi[\Psi^{\text{rec}}]$ was discretized and written as follows:

$$\text{Cost}[\mathcal{I}_1, \Psi^{\text{rec}}] = -d\sum_{j=1}^{J} |\mathcal{I}_1\left(y_j, \Psi^{\text{rec}}\right)|^4 + \zeta\sum_{n=1}^{N^{\text{rec}}} k_n^2\left(\left(p^{\text{rec}}_n\right)^2 + \left(q^{\text{rec}}_n\right)^2\right), \tag{26}$$



1944799x, 2025, 2, Downloaded from https://agupubs.onlinelibrary.wiley.com/doi/10.1029/2024RS008168, Wiley Online Library on [22/02/2025]. See the Terms and Conditions (https://onlinelibrary.wiley.com/terms-and-conditions) on Wiley Online Library for rules of use; OA articles are governed by the applicable Creative Commons License

where $y_j$ are the image sampling points, $1 \le j < J$, $d$ is the discretization step, and $p_n^{\text{rec}}$ and $q_n^{\text{rec}}$ are the coefficients in Equation 25.

To extend the variational approach of Gilman and Tsynkov (2023b) to the case of $K$ range bins, we replace the first term on the right-hand side of Equation 26 with the average of $\text{Cost}_{\mathcal{I}}\left[\mathcal{I}_1^{(k)}\right] = -\|\mathcal{I}_1^{(k)}\|_4^4$, which yields:

$$\text{Cost}_K\left[\left\{\mathcal{I}_1^{(k)}\right\}, \Psi^{\text{rec}}\right] = -\frac{d}{K}\sum_{k=1}^{K}\sum_{j=1}^{J}|\mathcal{I}_1^{(k)}(y_j, \Psi^{\text{rec}})|^4 + \zeta\sum_{n=1}^{N^{\text{rec}}}k_n^2\left(\left(p_n^{\text{rec}}\right)^2 + \left(q_n^{\text{rec}}\right)^2\right). \tag{27}$$

The minimization of the cost function Equation 27 is performed using an interior-point method implemented via the MATLAB `fmincon` function with an explicitly specified gradient and the initial guess $p_n^{\text{rec}} = q_n^{\text{rec}} = 0$ for all $n$, see Equation 25. Given that in general, neither $\text{Cost}[\mathcal{I}_1, \Psi^{\text{rec}}]$ of Equation 26 nor $\text{Cost}_K\left[\left\{\mathcal{I}_1^{(k)}\right\}, \Psi^{\text{rec}}\right]$ of Equation 27 can be expected to be convex, a gradient-based optimizer started from a single initial guess may converge to a local minimum rather than global minimum. To mitigate this problem, the multi-start optimization can be employed. Several examples of using it for transionospheric autofocus can be found in Gilman and Tsynkov (2023b).

## 6. Screen Projection Autofocus

For the point scatterer reflectivity function $\mu(z) = \mu_0\delta(z - z_0)$, Equations 1 and 8 lead to the expression given by Equation 17 for the partially focused image. It is possible to eliminate the unknown $z_0$ and $\mu_0$ from Equation 17 by differentiating with respect to $s$:

$$\left(\angle p_{\text{clean}}(s)\right)'' \approx \frac{2\pi}{\xi F} = \text{const}, \tag{28}$$

where $\angle$ denotes the complex phase, that is, argument of a complex number.

When $\Psi \neq 0$, the equality in Equation 28 is no longer guaranteed. However, one can introduce a correction by extending the analogy between the unperturbed screen projected data given by Equation 17 and signal at screen elevation, see Equation 18, to the case where the perturbation $\Psi$ is present. Namely, with $\Psi \neq 0$ the signal right above the screen elevation, that is, at $\xi + 0$, would become (cf. Equation 18):

$$\begin{aligned} u_\xi(s) &= \int_{s-\xi F/2}^{s+\xi F/2} \exp\left(\mathrm{i}\pi(s-z)^2/\xi F\right)\exp(-\mathrm{i}\Psi(s))\mu_0\delta(z-z_0)\,\mathrm{d}z \\ &= \mu_0\left[\exp\left(\frac{\mathrm{i}\pi(s-z_0)^2}{\xi F}\right)\exp(-\mathrm{i}\Psi(s))\right] \quad \text{for} \quad |s-z_0| \le \xi F/2. \end{aligned} \tag{29}$$

Taking the complex phase in Equation 29 and differentiating twice w.r.t. $s$, we obtain:

$$\left(\angle u_\xi(s)\right)'' = \frac{2\pi}{\xi F} - \left(\Psi(s)\right)''. \tag{30}$$

As, however, $u_\xi(s)$ is not available, we replace it with the partially focused image $p(s)$ of Equation 8. (Approximation of $u_\xi(s)$ by $p(s)$ involves corruption of the screen projected data, as analyzed in Appendix A.) Then, one can define the phase correction as

$$\left(\Psi^{\text{rec}}(s)\right)'' = \frac{2\pi}{\xi F} - \left(\angle p(s)\right)''. \tag{31}$$

We can integrate Equation 31 twice and substitute the resulting $\Psi^{\text{rec}}(s)$ into the second part (9) of the two-step reconstruction algorithm.



1944799x, 2025, 2, Downloaded from https://agupubs.onlinelibrary.wiley.com/doi/10.1029/2024RS008168, Wiley Online Library on [22/02/2025]. See the Terms and Conditions (https://onlinelibrary.wiley.com/terms-and-conditions) on Wiley Online Library for rules of use; OA articles are governed by the applicable Creative Commons License

Instead of obtaining $\Psi^{\text{rec}}$ from Equation 31 for a single chosen range bin, one can apply any established autofocus technique to the image (9), for example, map drift (Jakowatz et al., 1996) or phase curvature autofocus (PCA) (Wahl et al., 1994). This can be done when data from multiple range bins are available because most autofocus algorithms use it to enable iterative refinement and average out the effects of clutter and noise in each individual bin. Our implementation of PCA is as follows.

1. A uniform discretization grid $s_m$ is introduced for the screen coordinate $s$ with size $\Delta s$ on the order of or smaller than azimuthal resolution:

$$s_{m+1} - s_m = \Delta s \lesssim 1.$$

2. A partially focused image $p^{(k)}(s_m)$ is obtained for each range bin $k$, $1 \le k \le K$, by applying Equation 8 to Equation 24.
3. A relative signal magnitude threshold $Q_p$ is introduced, $0 < Q_p < 1$.
4. Domains of strong signal $\mathfrak{S}^{(k)}$ are defined for each range bin $k$:

$$\mathfrak{S}^{(k)} = \left\{s_m \;||p^{(k)}(s_{m+l})| \ge Q_p \max_m |p^{(k)}(s_m)| \text{ for } l \in \{-1, 0, 1\}\right\}. \tag{32}$$

In Equation 32, we require that the magnitude of the screen-projected signal $p^{(k)}$ be sufficiently high at the grid node $s_m$ and its two immediate neighbors, $s_{m-1}$ and $s_{m+1}$.

5. For each $m$, let $\mathcal{K}_m \overset{\text{def}}{=} \{k | s_m \in \mathfrak{S}^{(k)}\}$. Then, we build three vectors $\boldsymbol{p}_{am}$, $\boldsymbol{p}_{bm}$, and $\boldsymbol{p}_{cm}$ for each $m$ by stacking $p^{(k)}(s_{m-1})$, $p^{(k)}(s_m)$, and $p^{(k)}(s_{m+1})$, respectively, for all $k \in \mathcal{K}_m$.
6. Second derivatives on the grid are convenient to approximate by central differences:

$$(\angle p(s_m))'' \approx \frac{\angle p(s_{m-1}) - 2\angle p(s_m) + \angle p(s_{m+1})}{(\Delta s)^2}. \tag{33}$$

To approximate the entire Equation 31, we use the redundant data $\boldsymbol{p}_{am}, \boldsymbol{p}_{bm}, \boldsymbol{p}_{cm}$:

$$(\Psi^{\text{rec}}(s_m))'' \approx \frac{2\pi}{\xi F} - \frac{\angle\left((\boldsymbol{p}_{am} \circ \boldsymbol{p}_{cm}) \cdot (\bar{\boldsymbol{p}}_{bm} \circ \bar{\boldsymbol{p}}_{bm})\right)}{(\Delta s)^2}, \tag{34}$$

where $\circ$ denotes the Hadamard product of two vectors (component-wise), $\bar{\boldsymbol{p}}^*$ is the complex conjugate of a vector $\boldsymbol{p}$, and $\cdot$ is the conventional dot product of complex-valued vectors. To delineate Equation 34, we first notice that the subtrahend on the right-hand side of this equation can be expressed as follows:

$$\frac{\angle\left((\boldsymbol{p}_{am} \circ \boldsymbol{p}_{cm}) \cdot (\bar{\boldsymbol{p}}_{bm} \circ \bar{\boldsymbol{p}}_{bm})\right)}{(\Delta s)^2} = \frac{1}{(\Delta s)^2} \angle\left[\sum_{k \in \mathcal{K}_m} p^{(k)}(s_{m-1}) p^{(k)}(s_{m+1}) \left(\bar{p}^{(k)}(s_m)\right)^2\right]. \tag{35}$$

The complex phase of each individual term in the sum on the right-hand side of Equation 35 coincides with Equation 33:

$$\frac{1}{(\Delta s)^2} \angle\left(p^{(k)}(s_{m-1}) p^{(k)}(s_{m+1}) \left(\bar{p}^{(k)}(s_m)\right)^2\right) = \frac{\angle p^{(k)}(s_{m-1}) + \angle p^{(k)}(s_{m+1}) - 2\angle p^{(k)}(s_m)}{(\Delta s)^2}.$$

Yet the overall complex phase on the right-hand side of Equation 35 is not obtained as the average of individual phases. Instead, we first average the redundant complex-valued data by computing the full sum in Equation 35 and then take the argument of the result. It is in this sense that the data redundancy brought into Equation 34 by the vectors $\boldsymbol{p}_{am}, \boldsymbol{p}_{bm}$, and $\boldsymbol{p}_{cm}$ lets one combine the approximations to $(\Psi^{\text{rec}}(s_m))''$ from different range bins. This is similar to PGA that averages $(\angle p(s))'$ over multiple bins (Jakowatz et al., 1996, eqs. (4.39), (F.13)).



1944799x, 2025, 2, Downloaded from https://agupubs.onlinelibrary.wiley.com/doi/10.1029/2024RS008168, Wiley Online Library on [22/02/2025]. See the Terms and Conditions (https://onlinelibrary.wiley.com/terms-and-conditions) on Wiley Online Library for rules of use; OA articles are governed by the applicable Creative Commons License

7. Rather than integrating the right-hand side of Equation 34 twice, we derive $\Psi^{\text{rec}}$ using a different approach suggested by the Fourier representation in (25). We divide the Fourier transform of the right-hand side of Equation 34 by $-k_n^2$ and take the inverse transform.
8. The screen projected data are updated in all bins using the output of step 7. Namely,

$$p_{r+1}^{(k)}(s_m) = p_r^{(k)}(s_m)\exp\left(\mathrm{i}\Psi_r^{\text{rec}}(s_m)\right),$$

where $r$ is the iteration number.

We initialize the iteration by taking $\Psi_0^{\text{rec}} \equiv 0$ and $p_0^{(k)}(s_m)$ given by Equation 8 with $u^{(k)}(x)$ of Equation 24 substituted for $u(x)$. Then, steps 5 through 8 are performed repeatedly for $r = 0, 1, 2, \ldots$ In our simulations, we observed little improvement in the focusing quality after the first iteration. For this reason, we did not use any stopping criteria and performed a fixed number of iterations instead — repeated the steps 5 through 8 10 times.

Note that once $\Psi^{\text{rec}}$ has been obtained, it can also be used in the one-step reconstruction (2). However, since the focusing has been performed using the corrupted data $\{p^{(k)}(s)\}$ (see the discussion toward the end of Section 3, around Figures 3 and 5), we can expect that the resulting reconstruction phase $\Psi^{\text{rec}}(s)$ and corresponding images will inherit the corruption.

## 7. Numerical Simulations

In this section, we conduct a statistical analysis of the autofocus performance for the optimization-based and screen projection approaches described in Sections 5 and 6, respectively. We generate a set of reflectivity functions $\{\mu^{(k)}\}$, $1 \le k \le 250$, each representing a single range bin. Each $\mu^{(k)}$ contains clutter and a single point scatterer at a random location, see Equation 23. We also generate a set of phase screens $\Psi_{(m)}(s)$, $1 \le m \le 30$, by taking random i.i.d. $\varphi_n$ for all $n$ in Equation 6. The Fourier amplitudes of each phase screen are scaled to achieve a predefined value of $a_s$, see Equation 7. Then the resulting set of phase screens is combined with the set of reflectivities $\{\mu^{(k)}\}$, where the level of clutter in Equation 23 is also scaled to a predefined value. When calculating the antenna signal using Equation 24, the noise level is taken equal to that of clutter. This way, we obtain a set of antenna signals $\mathcal{U} = \{u^{(k)}(x;\Psi_{(m)})\}$ parametrized by the values of $a_s$ and $a_{\text{clutter}} = a_{\text{noise}}$, that is, $\mathcal{U} = \mathcal{U}(a_{\text{clutter}}, a_s)$. Hence, for each pair $(a_{\text{clutter}}, a_s)$, the set $\mathcal{U}(a_{\text{clutter}}, a_s)$ contains $30 \times 250$ simulated antenna signals $u(x)$. Other parameters of the simulation setup are as follows: $\xi = 0.5$, $F = 100$, $N = N^{\text{rec}} = 6$, $k_1 = 1.5 \cdot (2\pi/F)$, $k_n = nk_1$, $a_n = (k_1/k_n)^2 a_1$, see (Gilman & Tsynkov, 2023b) for more details (see also a short discussion following (7) regarding the $C_k L$-based characterization of the turbulence level).

For each $u^{(k)}(x;\Psi_{(m)})$, we calculate the one-dimensional images using the optimization-based and screen projection autofocus, as well as the perfect reconstruction, that is, $\Psi^{\text{rec}} \equiv \Psi_{(m)}$. In each image we locate the peak due to the point scatterer and, similarly to Figure 5, extract three peak metrics: FWHM, ISLR, and peak height. These metrics, averaged over $\mathcal{U}(a_{\text{clutter}}, a_s)$, are used in Figure 6 to compare the performance of the two focusing algorithms. Each colored panel in Figure 6 consists of $5 \times 6$ colored tiles, where each tile represents a certain pair of values $(a_{\text{clutter}}, a_s)$. The value of the metric averaged over $\mathcal{U}(a_{\text{clutter}}, a_s)$ is shown using the color scale next to the panel. The top and middle row of panels correspond to the optimization-based and screen projection algorithms, respectively, while the bottom row shows a signed difference between the two. The optimization-based algorithm yields smaller values of FWHM and ISLR and larger peak heights compared to the screen projection, which indicates its overall superior performance.

Similar graphics can be used to assess the performance of the focusing algorithms individually. To do so for the optimization-based method, we replace the second row in Figure 6 with the one that corresponds to the exact reconstruction of $\Psi(s)$ in (2), that is, $\mathcal{I}_1[\Psi, \Psi]$. The result is shown in Figure 7 where we see that the color scale values in the third row of panels turn positive, meaning that the performance of the optimization-based approach is inferior to the perfect reconstruction (as one could expect). Yet we observe a significantly smaller differences in performance metrics in this plot as compared to Figure 6, especially for $a_s \le 0.8\pi$ (see the fourth row of panels in Figure 7).



19447799x, 2025, 2, Downloaded from https://agupubs.onlinelibrary.wiley.com/doi/10.1029/2024RS008168, Wiley Online Library on [23/02/2025]. See the Terms and Conditions (https://onlinelibrary.wiley.com/terms-and-conditions) on Wiley Online Library for rules of use; OA articles are governed by the applicable Creative Commons License

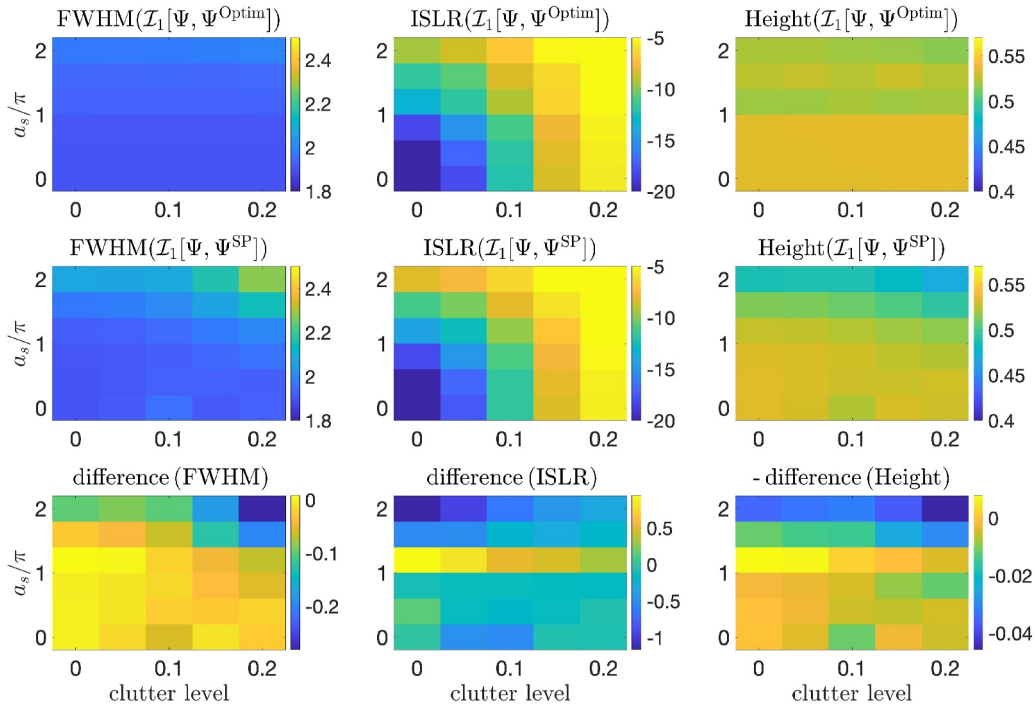


**Figure 6.** Autofocus performance metrics averaged over $\mathcal{U}(a_{\text{clutter}}, a_s)$ as functions of $a_{\text{clutter}}$ (the $x$-axis) and $a_s$ ($y$-axis), see Equations 7 and 22, respectively. Left column of panels: FWHM, center column: ISLR, right column: peak height. Top row of panels: optimization-based focusing $(\Psi^{\text{Optim}})$; middle row: screen projection focusing $(\Psi^{\text{SP}})$; bottom row: signed difference between the top and middle rows, with the sign as indicated in the panel titles. Note that the negative sign is taken for the bottom right panel because the deterioration of the image is accompanied by the increate in FWHM and ISLR and decrease in the peak height, so this sign choice makes the color patterns in the bottom row consistent.

Another way to characterize the focusing performance is to analyze the worst case scenarios rather than consider averages over $\mathcal{U}(a_{\text{clutter}}, a_s)$. For example, the largest performance decrease of optimization-based autofocus as compared to perfect reconstruction (i.e., $\Psi^{\text{rec}} = \Psi$) in the case of $\mathcal{U}(0.2, 0.8\pi)$ is 0.006 for FWHM, 0.06 for ISLR, and 0.001 for peak height. These values are very small and indicate that at this level of perturbations and clutter the optimization algorithm still works well even if there could be local minima of $\text{Cost}_K$ (see (Gilman & Tsynkov, 2023b) for more detail). The corresponding focusing deterioration by the screen projection algorithm is 1.3 for FWHM, 3.0 for ISLR, and 0.1 for peak height. These values are significantly larger. In Figure 8, we are showing an example of reconstruction using the two autofocus techniques. This case corresponds to the largest deterioration of ISLR demonstrated by $\mathcal{I}_1\left[\Psi, \Psi^{\text{SP}}\right]$ over the set $\mathcal{U}(0.2, 0.8\pi)$.

Altogether, the optimization-based autofocus yields a much better quality of focusing than the screen projection does, at least for $a_s \lesssim 0.8\pi$. However, for higher amplitudes of perturbations a simple gradient-based optimizer can converge to a local rather than global minimum of $\text{Cost}_K$. One such example from $\mathcal{U}(0.12, 2\pi)$ (i.e., $a_s = 2\pi$) is shown in Figure 9. In this case, the screen projection autofocus outperforms optimization, at least in terms of how the phase screen density is reconstructed. This apparently implies that replacing the single-bin cost function (26) with the multi-bin cost function (27) does not eliminate the problem of local minima (Gilman & Tsynkov, 2023b). Local minima are a manifestation of non-convexity of the cost function. In Gilman & Tsynkov (2023b), we have shown that this issue can be mitigated substantially by multi-start optimization, but with a considerable increase in computational expense. In the future, we plan to look into employing other, more efficient optimization strategies for the cost functions given by Equations 26 and 27.

## 8. Conclusions

We have evaluated and compared the performance of transionospheric SAR autofocus for two different methods. The first method is an extension of the optimization-based procedure developed in our earlier work (Gilman & Tsynkov, 2023b) to the case of multiple range bins. The second approach, proposed in Ji et al. (2022), is a screen



1944799x, 2025, 2, Downloaded from https://agupubs.onlinelibrary.wiley.com/doi/10.1029/2024RS008168, Wiley Online Library on [23/02/2025]. See the Terms and Conditions (https://onlinelibrary.wiley.com/terms-and-conditions) on Wiley Online Library for rules of use; OA articles are governed by the applicable Creative Commons License

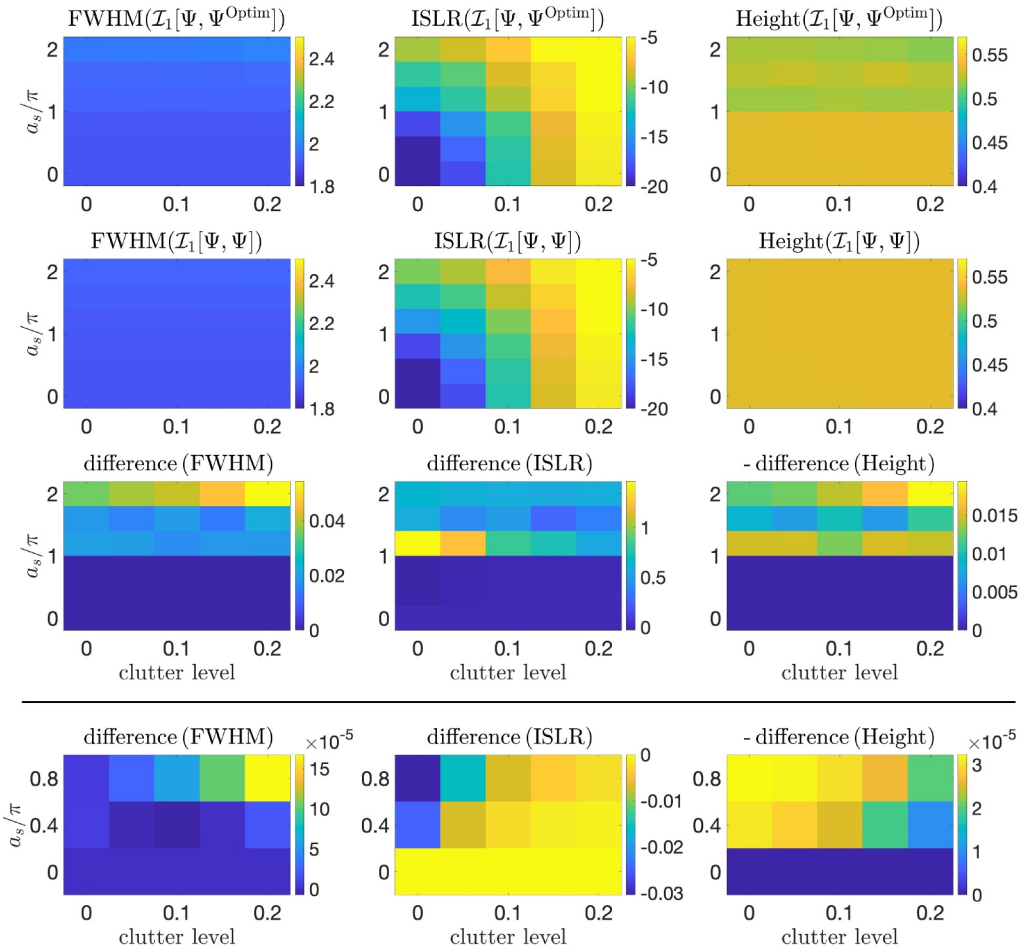


**Figure 7.** Same as Figure 6, but with exact reconstruction of $\Psi$ instead of the screen projection autofocus in the second row. The fourth row is a zoom-in on the third row for $0 \leq a_s/\pi \leq 0.8$.

projection method where the phase curvature autofocus (PCA) is applied to the antenna signal migrated to the phase screen elevation. The screen projection method that does not involve optimization was considered an alternative to the variational autofocus, where the computational cost of solving the optimization problem could be rather high, especially when one uses the multi-start optimization to mitigate the non-convexity. The autofocus performance has been evaluated statistically for a range of simulated target reflectivities and phase screen density functions, with perfect reconstruction of phase perturbations being a baseline. Our findings can be summarized as follows.

1. Migration of the antenna signal to phase screen elevation corrupts the data so that even with perfect reconstruction of phase perturbations, the quality of the images obtained using the screen projection method is degraded. This effect rapidly intensifies as the magnitude of perturbations increases.
2. For low and moderate levels of phase perturbations ($a_s \lesssim 0.8\pi$), the optimization-based autofocus performs on par with perfect reconstruction of phase perturbations. Its performance is superior to that of the screen projection method.
3. For higher levels of phase perturbations, the performance of both methods deteriorates.
4. The problem of non-convexity of the cost function in optimization-based autofocus observed in Gilman & Tsynkov (2023b) for a single range bin persists for multiple range bins.

In the future, we will try and improve the performance of both methods analyzed in this study. Note that the iterative focusing procedure used for the screen projection method, see Section 6, is applied to the migrated data that is subject to a significant corruption, as per Equation 21. The same migrated (and corrupted) data is used on



1944799x, 2025, 2, Downloaded from https://agupubs.onlinelibrary.wiley.com/doi/10.1029/2024RS008168, Wiley Online Library on [23/02/2025]. See the Terms and Conditions (https://onlinelibrary.wiley.com/terms-and-conditions) on Wiley Online Library for rules of use; OA articles are governed by the applicable Creative Commons License

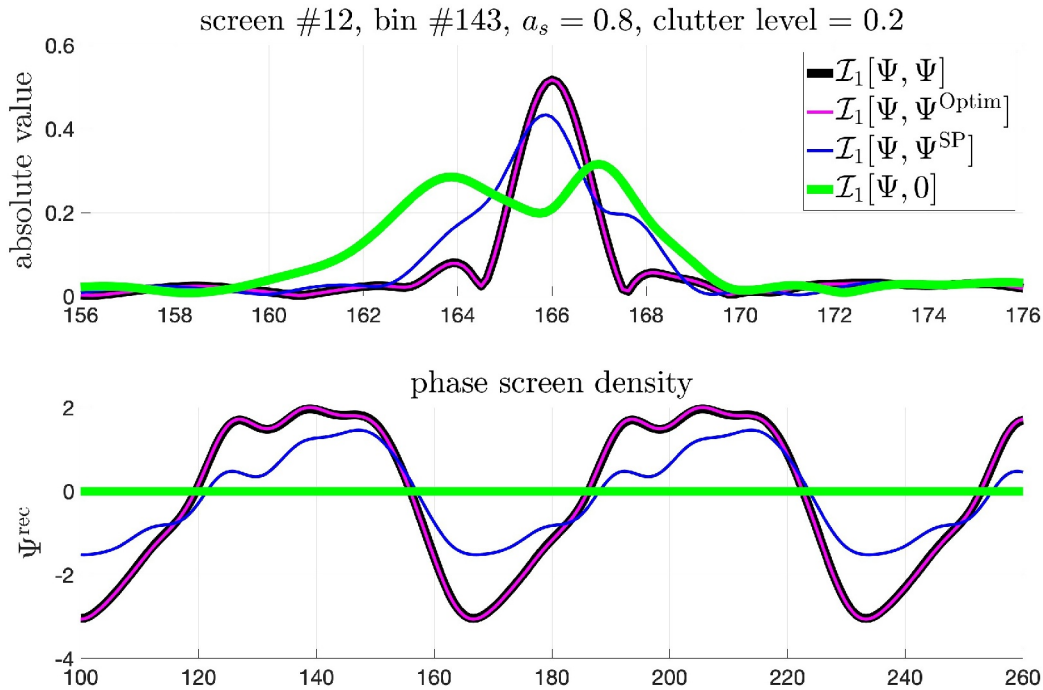


**Figure 8.** The worst-case scenario for the screen projection autofocus and $a_s = 0.8\pi$. Top plot: zoom-ins to the peaks of $I(y)$ due to a point scatterer; the notations in the legend are similar to those in Figure 4. Bottom plot: the corresponding phase screen density functions $\Psi^{\mathrm{rec}}(s)$ used to produce the images in the top plot. As in Figure 4, the unit along the horizontal axis is the resolution size $\Delta_{\mathrm{A}}$ given by Equation 3. The horizontal scales are different on the top and bottom plots.

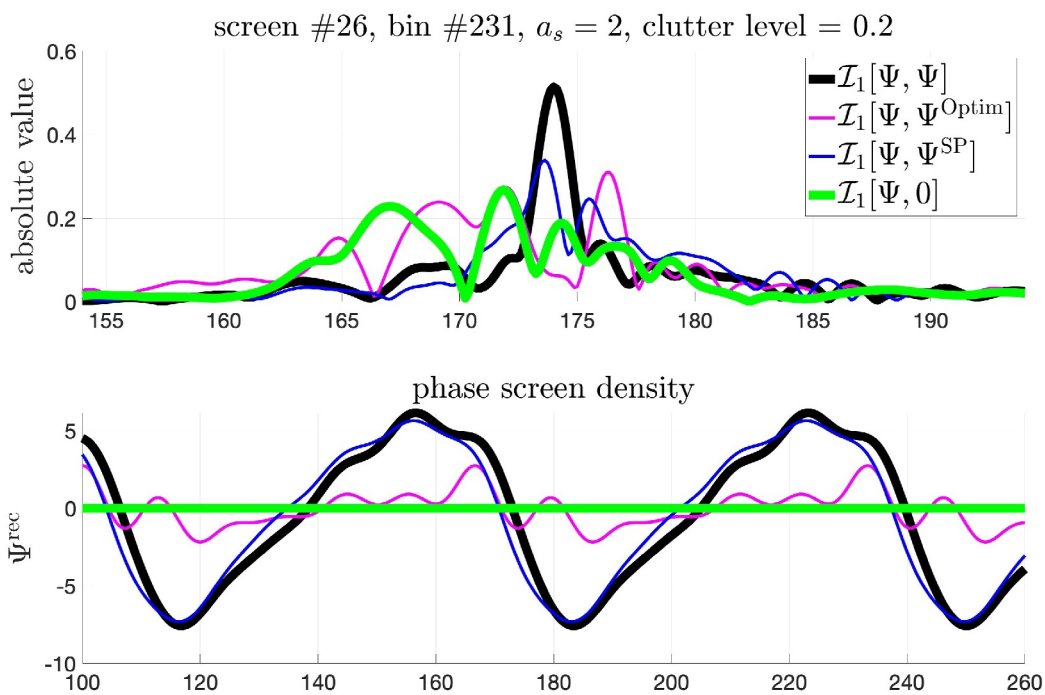


**Figure 9.** Similar to Figure 8: the worst-case scenario for the optimization-based autofocus and $a_s = 2\pi$.



1944799x, 2025, 2, Downloaded from https://agupubs.onlinelibrary.wiley.com/doi/10.1029/2024RS008168, Wiley Online Library on [22/02/2025]. See the Terms and Conditions (https://onlinelibrary.wiley.com/terms-and-conditions) on Wiley Online Library for rules of use; OA articles are governed by the applicable Creative Commons License

1944799x, 2025, 2, Downloaded from https://agupubs.onlinelibrary.wiley.com/doi/10.1029/2024RS008168, Wiley Online Library on [22/02/2025]. See the Terms and Conditions (https://onlinelibrary.wiley.com/terms-and-conditions) on Wiley Online Library for rules of use; OA articles are governed by the applicable Creative Commons License

every iteration. We will see whether the migration procedure can be adjusted to take into account the current approximation of the phase screen density function, thus reducing the corruption of the migrated data with iterations and improving the method's overall performance. The main obstacle to such a development is that unlike in the full waveform inversion (see, e.g., (Churchill & Gelb, 2022)), the result of focusing is the image $\mathcal{I}(y)$ rather than reflectivity function $\mu(z)$, and hence, Equation 1 cannot be used directly to provide phase corrections for the data $u(x)$.

For the optimization-based autofocus, we will explore modifications to the cost function, as well as different global optimization methods such as multi-start or genetic algorithms (MATLAB Global Optimization Toolbox, 2021). We will also extend the statistical approach adopted in this paper to explore the effect of other factors such as the wavenumber spectrum of perturbations and parameters of the simulated reflectivity functions. Some benefits could also be obtained by combining the two methods analyzed in this work. For example, we plan to check whether the screen projection method can provide a useful "initial guess" for the optimization-based method.

The main goal of this study is to compare two different autofocus methods. To render the comparison in a most efficient way, we make several assumptions that may limit the applicability of our results to other situations. First, even though multiple range bins provide the data in this work, the reconstructed phase screen still remains one-dimensional. Potentially, two-dimensional phase screens can be obtained as an outcome of autofocus. However, in that case the algorithms should take into account the exact arrangement of the bins and range cell migration (Cumming & Wong, 2005). Hence, the results of this work are not directly applicable to the analysis of efficiency of phase screen reconstruction. Another limitation comes from the target model that includes isolated point scatterers, whereas low-frequency SAR missions are typically designed for forest and ice applications and we may expect that point-like scatterers in such images will be relatively rare. Hence, the focusing success rates reported in this paper cannot be immediately used to predict the expected accuracy of reconstruction of the phase screen or any other ionospheric quantities. Lifting these limitations is yet another future objective.

## Appendix A: Screen Level Signal Versus Partially Focused Image

In this section, we analyze the effect of corruption of the screen projected data, see Figure 3 and the accompanying discussion. We depart from Equation 18 describing the signal $u_\xi(s)$ that corresponds to the case of no perturbations and antenna trajectory at screen elevation. Introducing the perturbation $\Psi$ and taking a single point scatterer $\mu(z) = \mu_0\delta(z - z_0)$ as the target, we obtain a new expression for the signal:

$$u_\xi(s) = \mu_0 \exp\left(\frac{\mathrm{i}\pi(s - z_0)^2}{\xi F}\right) \exp(-\mathrm{i}\Psi(s)) \cdot \mathbf{1}_{|s-z_0|\le \xi F/2}, \tag{A1}$$

where $\mathbf{1}_{|s-z_0|\le \xi F/2}$ is the characteristic function of the interval $z_0 - \xi F/2 \le s \le z_0 + \xi F/2$. Our goal is to compare Equation A1 with the partially focused image $p(s)$ given by Equation 8.

By defining $s(x) \equiv s(x, z_0)$, see Equation 4, we can derive the following relation between $u_\xi(s)$ and the antenna signal $u(x)$ due to the same reflectivity function $\mu(z) = \mu_0\delta(z - z_0)$:

$$u(x) = u_\xi(s(x)) \exp\left(\frac{\mathrm{i}\pi\eta(x - z_0)^2}{F}\right) \cdot \mathbf{1}_{|x-z_0|\le F/2}, \tag{A2}$$

where $\eta = 1 - \xi$. To avoid confusion, hereafter we will use the variable $r$ as the argument of $p$. Substituting Equation A2 into Equation 8 and dropping inessential constant factors, we obtain

$$p(r) \propto \int_{r-\eta F/2}^{r+\eta F/2} u_\xi(s(x)) \exp\left(\frac{\mathrm{i}\pi\eta(x - z_0)^2}{F}\right) \exp\left(\frac{-\mathrm{i}\pi[x - r]^2}{\eta F}\right) \cdot \mathbf{1}_{|x-z_0|\le F/2}\, \mathrm{d}x. \tag{A3}$$

Defining $x(s)$ as an inverse to $s(x)$, substituting Equation A1 into Equation A3, and making a change of the integration variable, we arrive at

$$p(r) \propto \int \exp\left(\frac{\mathrm{i}\pi(s-z_0)^2}{\xi F}\right) \exp(-\mathrm{i}\Psi(s)) \cdot \mathbf{1}_{|s-z_0|\le \xi F/2} \exp\left(\frac{\mathrm{i}\pi\eta[x(s)-z_0]^2}{F}\right) \exp\left(\frac{-\mathrm{i}\pi[x(s)-r]^2}{\eta F}\right) \cdot \mathbf{1}_{|x(s)-z_0|\le F/2}\, \mathrm{d}s, \tag{A4}$$

where the integration limits are defined by the characteristic functions $\mathbf{1}_{|s-z_0|\le \xi F/2}$ and $\mathbf{1}_{|x(s)-z_0|\le F/2}$ in the integrand.

In the absence of perturbations, the coordinate-dependent part of $p(r)$ is given by Equation 17:

$$p_{\mathrm{clean}}(r) \propto \exp\left(\frac{\mathrm{i}\pi(r-z_0)^2}{\xi F}\right). \tag{A5}$$

We would like to see how the phase in Equation A5 is perturbed due to $\Psi(s)$. To do so, we multiply Equation A4 with the complex conjugate of Equation A5, which yields:

$$\begin{aligned} q(r) \equiv\ & p(r)\exp\left(-\frac{\mathrm{i}\pi(r-z_0)^2}{\xi F}\right) \\ \propto\ & \int \exp(-\mathrm{i}\Psi(s)) \exp(\mathrm{i}\Phi) \cdot \mathbf{1}_{|s-z_0|\le \xi F/2} \cdot \mathbf{1}_{|x(s)-z_0|\le F/2}\, \mathrm{d}s. \end{aligned} \tag{A6}$$

The general expression for the phase term $\Phi$ in Equation A6 is cumbersome. We will calculate it for a particular case of $\xi = \eta = 1/2$, that is, when the phase screen is at half of the orbit elevation. Introducing

$$\tilde{r} = r - z_0, \quad \tilde{s} = s - z_0,$$

we can show that

$$\Phi\Big|_{\xi=1/2} = -4\frac{\pi}{F}(\tilde{r}-\tilde{s})^2. \tag{A7}$$

Combining Equations A6 and A7 and noticing that $\tilde{r} - \tilde{s} = r - s$, we obtain

$$q(r)\Big|_{\xi=1/2} \propto \int \exp(-\mathrm{i}\Psi(s))\, K(r,s)\, \mathrm{d}s, \tag{A8}$$

where

$$K(r,s) = \exp\left(-4\mathrm{i}\frac{\pi(r-s)^2}{F}\right) \cdot \mathbf{1}_{|s-z_0|\le \xi F/2} \cdot \mathbf{1}_{|x(s)-z_0|\le F/2}. \tag{A9}$$

From Equation A8, we see that unlike in Equation A1, the perturbation of the partially focused image, that is, $q(s)$, is not equivalent to the complex exponential $\exp(-\mathrm{i}\Psi(s))$. It is rather obtained from the latter via convolution with the kernel Equation A9. It is this convolution that defines corruption of the screen projected data. Its subsequent analysis based on Equations A6, A8, and A9 may help one obtain a more accurate estimate of phase distortions compared to that given by Equation 21, but this analysis is beyond the scope of the current work.

## Data Availability Statement

Data were neither used nor created for this research.



1944799x, 2025, 2, Downloaded from https://agupubs.onlinelibrary.wiley.com/doi/10.1029/2024RS008168, Wiley Online Library on [22/02/2025]. See the Terms and Conditions (https://onlinelibrary.wiley.com/terms-and-conditions) on Wiley Online Library for rules of use; OA articles are governed by the applicable Creative Commons License

**Acknowledgments**
This work is supported by the US Air Force Office of Scientific Research (AFOSR) under awards number FA9550-23-1-0101 and FA9550-24-1-0172.

## References

Betancourt-Payan, F., Rodriguez-Cassola, M., Benedikter, A., Prats-Iraola, P., & Krieger, G. (2022). An autofocus algorithm for the recovery of ionospheric phase signatures in the Biomass mission. In *EUSAR 2022; 14th European conference on synthetic aperture radar* (pp. 1–5).

Biomass ESA's forest mission. (2024). Retrieved from https://www.esa.int/Applications/Observing_the_Earth/FutureEO/Biomass

Carrano, C. S., Groves, K. M., & Caton, R. G. (2012). Simulating the impacts of ionospheric scintillation on L band SAR image formation. *Radio Science*, *47*(04), 1–14. https://doi.org/10.1029/2011rs004956

Churchill, V., & Gelb, A. (2022). Sampling-based spotlight SAR image reconstruction from phase history data for speckle reduction and uncertainty quantification. *SIAM/ASA Journal on Uncertainty Quantification*, *10*(3), 1225–1249. https://doi.org/10.1137/20m1379721

Cumming, I. G., & Wong, F. H. (2005). *Digital processing of synthetic aperture radar data algorithms and implementation*. Artech House.

Fienup, J., & Miller, J. (2003). Aberration correction by maximizing generalized sharpness metrics. *Journal of the Optical Society of America A*, *20*(4), 609–620. https://doi.org/10.1364/josaa.20.000609

Garnier, J., & Sølna, K. (2013). A multiscale approach to synthetic aperture radar in dispersive random media. *Inverse Problems*, *29*. https://doi.org/10.1088/0266-5611/29/5/054006

Gilman, M., Smith, E., & Tsynkov, S. (2017). *Transionospheric synthetic aperture imaging*. Birkhäuser/Springer. https://doi.org/10.1007/978-3-319-52127-5

Gilman, M., & Tsynkov, S. (2017). Mathematical analysis of SAR imaging through a turbulent ionosphere. In M. D. Todorov (Ed.), *Application of mathematics in technical and natural sciences: 9th international conference for promoting the application of mathematics in technical and natural sciences—Amitans'17* (Vol. 1895, p. 23). https://doi.org/10.1063/1.5007357

Gilman, M., & Tsynkov, S. (2023a). Vertical autofocus for the phase screen in a turbulent ionosphere. *Inverse Problems*, *39*(4), 36. https://doi.org/10.1088/1361-6420/acb8d6

Gilman, M., & Tsynkov, S. (2024). Modeling the Earth's ionosphere by a phase screen for the analysis of transionospheric SAR imaging. *IEEE Transactions on Geoscience and Remote Sensing*, *62*, 1–16. https://doi.org/10.1109/TGRS.2023.3335146

Gilman, M., & Tsynkov, S. V. (2023b). Transionospheric autofocus for synthetic aperture radar. *SIAM Journal on Imaging Sciences*, *16*(4), 2144–2174. https://doi.org/10.1137/22M153570X

Gomba, G., Parizzi, A., De Zan, F., Eineder, M., & Bamler, R. (2015). Toward operational compensation of ionospheric effects in SAR interferograms: The split-spectrum method. *IEEE Transactions on Geoscience and Remote Sensing*, *54*(3), 1446–1461. https://doi.org/10.1109/tgrs.2015.2481079

Heliere, F., Fois, F., Arcioni, M., Bensi, P., Fehringer, M., & Scipal, K. (2014). Biomass P-band SAR interferometric mission selected as 7th Earth explorer mission. In *Proceedings of the 10th european conference on synthetic aperture radar, EUSAR 2014* (pp. 1–4).

Jakowatz, C. V., Jr., Wahl, D. E., Eichel, P. H., Ghiglia, D. C., & Thompson, P. A. (1996). *Spotlight-mode synthetic aperture radar: A signal processing approach*. Springer.

Ji, Y., Dong, Z., Zhang, Y., Wang, C., Hu, C., & Xu, Z. (2024). Transionospheric synthetic aperture radar observation: A comprehensive review. *IEEE Geoscience and Remote Sensing Magazine*, 2–43. https://doi.org/10.1109/MGRS.2024.3454635

Ji, Y., Yu, C., Zhang, Q., Dong, Z., Zhang, Y., & Wang, Y. (2022). An ionospheric phase screen projection method of phase gradient autofocus in spaceborne SAR. *IEEE Geoscience and Remote Sensing Letters*, *19*, 1–5. https://doi.org/10.1109/lgrs.2022.3147036

Kim, J. S., Papathanassiou, K. P., Scheiber, R., & Quegan, S. (2015). Correcting distortion of polarimetric SAR data induced by ionospheric scintillation. *IEEE Transactions on Geoscience and Remote Sensing*, *53*(12), 6319–6335. https://doi.org/10.1109/tgrs.2015.2431856

Li, Z., Quegan, S., Chen, J., & Rogers, N. C. (2015). Performance analysis of phase gradient autofocus for compensating ionospheric phase scintillation in BIOMASS P-band SAR data. *IEEE Geoscience and Remote Sensing Letters*, *12*(6), 1367–1371. https://doi.org/10.1109/lgrs.2015.2402833

MATLAB Global Optimization Toolbox. (2021). The MathWorks, Natick, MA, USA.

Meyer, F. J., Chotoo, K., Chotoo, S. D., Huxtable, B. D., & Carrano, C. S. (2016). The influence of equatorial scintillation on L-band SAR image quality and phase. *IEEE Transactions on Geoscience and Remote Sensing*, *54*(2), 869–880. https://doi.org/10.1109/tgrs.2015.2468573

Morrison, R. L., Do, M. N., & Munson, D. C. (2007). SAR image autofocus by sharpness optimization: A theoretical study. *IEEE Transactions on Image Processing*, *16*(9), 2309–2321. https://doi.org/10.1109/tip.2007.903252

Muller, R. A., & Buffington, A. (1974). Real-time correction of atmospherically degraded telescope images through image sharpening. *Journal of the Optical Society of America A*, *64*(9), 1200–1210. https://doi.org/10.1364/josa.64.001200

Pi, X. (2015). Ionospheric effects on spaceborne synthetic aperture radar and a new capability of imaging the ionosphere from space. *Space Weather*, *13*(11), 737–741. https://doi.org/10.1002/2015SW001281

Reeves, G., Colvin, T. J., & Locke, J. (2019). Next step space weather benchmarks (IDA Group Report No. NS GR-10982). 1701 Pennsylvania Ave. In *Suite 500 Washington, DC 20006-3602: Institute for defense analyses, science & Technology Policy Institute*. Retrieved from https://www.ida.org/-/media/feature/publications/n/ne/next-step-space-weather-benchmarks/gr-10982.ashx

Rino, C. (1979). A power law phase screen model for ionospheric scintillation: 1. Weak scatter. *Radio Science*, *14*(6), 1135–1145. https://doi.org/10.1029/rs014i006p01135

Secan, J. A., & Bussey, R. M. (1994). *An improved model of high-latitude f-region scintillation (wbmod version 13). (Tech. Rep.)*. BELLEVUE WA: NORTHWEST RESEARCH ASSOCIATES INC.

Tippie, A. E., & Fienup, J. R. (2009). Phase-error correction for multiple planes using a sharpness metric. *Optics Letters*, *34*(5), 701–703. https://doi.org/10.1364/ol.34.000701

Wahl, D. E., Jakowatz, C. V., Jr., Thompson, P. A., & Ghiglia, D. C. (1994). New approach to strip-map SAR autofocus. In *Sixth IEEE digital signal processing workshop, 1994* (pp. 53–56).



1944799x, 2025, 2, Downloaded from https://agupubs.onlinelibrary.wiley.com/doi/10.1029/2024RS008168, Wiley Online Library on [22/02/2025]. See the Terms and Conditions (https://onlinelibrary.wiley.com/terms-and-conditions) on Wiley Online Library for rules of use; OA articles are governed by the applicable Creative Commons License